The Dependence of Dark Matter Halo Properties on the Morphology of Their Central Galaxies from Weak Lensing

Zhenjie Liu [ID],[1, 2] Kun Xu [ID],[3, 1, 4] Jun Zhang,[1, 5] Wenting Wang,[1] and Cong Liu[1]

[1]*Department of Astronomy, Shanghai Jiao Tong University, Shanghai 200240, China*
[2]*Division of Physics and Astrophysical Science, Graduate School of Science, Nagoya University, Nagoya 464-8602, Japan*
[3]*Center for Particle Cosmology, Department of Physics and Astronomy, University of Pennsylvania, Philadelphia, PA 19104, USA*
[4]*Institute for Computational Cosmology, Department of Physics, Durham University, South Road, Durham DH1 3LE, UK*
[5]*Shanghai Key Laboratory for Particle Physics and Cosmology, Shanghai 200240, China*

ABSTRACT

Xu & Jing (2022) reported a monotonic relationship between host halo mass (M_h) and the morphology of massive central galaxies, characterized by the Sérsic index (n), at fixed stellar mass, suggesting that morphology could serve as a good secondary proxy for halo mass. Since their results were derived using the indirect abundance matching method, we further investigate the connection between halo properties and central galaxy morphology using weak gravitational lensing. We apply galaxy-galaxy lensing to measure the excess surface density around CMASS central galaxies with stellar masses in the range of $11.3 < \log M_*/\mathrm{M_\odot} < 11.7$, using the HSC shear catalog processed through the Fourier_Quad pipeline. By dividing the sample based on n, we confirm a positive correlation between n and M_h, and observe a possible evidence of the positive correlation of n and halo concentration. After accounting for color, we find that neither color nor morphology alone can determine halo mass, suggesting that a combination of both may serve as a better secondary proxy. In comparison to hydrodynamic simulations, we find that TNG300 produce much weaker correlations between M_h and n. Furthermore, disabling jet-mode active galactic nuclei feedback in SIMBA simulations results in the disappearance of the positive $n - M_h$ relationship, suggesting that the star formation history influenced by black holes may be a contributing factor.

Keywords: weak lensing, morphology of galaxy, dark matter halo, Stellar-to-Halo Mass Relation

1. INTRODUCTION

In the ΛCDM cosmological model, the large-scale structure of the universe is shaped by the gravitational influence of dark matter, such as halos, filaments and voids. These dark matter halos subsequently act as "seeds" for galaxy formation. Dark matter, a substance that has not yet been directly observed, constitute the major mass of the universe, whereas stars are the luminous objects we can observe. The Stellar-to-Halo Mass Relation (SHMR) reveals the intimate connection between the stellar mass of galaxies and the mass of dark matter halos, indicating the link between galaxy formation and the evolution of dark matter halos. It is generally believed that massive dark matter halos host more massive galaxies. Therefore, by utilizing SHMR, we can assign galaxy masses to halos in N-body simulations, or infer halo mass from stellar mass. This allows for a deeper understanding of the evolutionary history of galaxies, and their coevolution with dark matter halos.

Although SHMR provides critical insights into the connection between galaxies and halos, it also exhibits significant scatter (Cooper et al. 2010; Xu et al. 2023; Zentner et al. 2014; Zu et al. 2021, 2022), primarily due to the influence of other galaxy properties such as size, color, and morphology. For instance, some studies find that halos of blue (star-forming) galaxies are less massive than those of red (quenched/passive) galaxies with the same stellar mass (Rodríguez-Puebla et al. 2015; Mandelbaum et al. 2016; Taylor et al. 2020; Wang et al. 2021; Xu & Jing 2022). Conversely, other studies (Tin-

Corresponding author: Zhenjie Liu, Kun Xu
liuzhj26@sjtu.edu.cn, kunxu@sas.upenn.edu

ker et al. 2013; Moster et al. 2018; Guo et al. 2019) report the opposite conclusion.

The morphology of galaxies is also found to correlate with halo mass. Galaxy morphology is typically described by the Sérsic profile (Sérsic 1963), which characterizes the brightness, size, and the morphology of a galaxy. The Sérsic profile is modeled as:

$$I(r) = I_e \exp\left\{ -b_n \left[\left(\frac{R}{R_e} \right)^{\frac{1}{n}} - 1 \right] \right\}, \qquad (1)$$

where b_n is defined through $\gamma(2n; b_n) = \Gamma(2n)$, Γ and γ are the Gamma function and the lower incomplete Gamma function, respectively. I_e is the surface brightness at the half-light radius R_e. The Sérsic index n quantifies the curvature of the galaxy's luminosity profile, with higher values indicating more concentrated core of light distributions. In this work, we focus on the relation between halo masses and the morphology of galaxies, characterized by the Sérsic index (n). Studies from Sonnenfeld et al. (2019) utilize lensing data from the Hyper Suprime-Cam Survey (HSC) to study the relationship between halo mass and stellar mass, galaxy size, and Sérsic index in the CMASS sample. They find no significant correlation between halo mass and size or Sérsic index at a fixed stellar mass. However, Taylor et al. (2020) find that for galaxies with a stellar mass of around $10^{10.5} \mathrm{M}_\odot$, the Sérsic index and effective radius are the best indicators of host halo mass, while showing weaker correlations with star formation rate or color. Applying the Photometric Objects Around Cosmic Webs (PAC; Xu et al. 2022) method, Xu & Jing (2022) find that more compact, red, and larger galaxies tend to be located in more massive halos. But their method of estimating halo mass relies on abundance matching, which assumes a one-to-one correspondence between stellar mass and the satellite distribution of the host halo. Therefore, the relationship between galaxy morphology and halo mass remains unclear, and the physical origin influencing the SHMR also remains an open question.

Weak gravitational lensing can serve as a crucial probe to the total mass of dark matter halos and the matter distribution, which distorts background galaxy images around massive objects, known as shear. Galaxy-galaxy lensing, in particular, can directly measure the average density profile of halos around galaxies or galaxy clusters, thus reflecting the halo mass. In this work, we utilize the lensing data from the third public data release of HSC to further analyze and discuss the dependence of the host halo mass on the morphology of massive central galaxies with stellar masses in the range of $11.3 < \log(M_*/\mathrm{M}_\odot) < 11.7$. We introduce our galaxy sample and shear catalog in Section 2, and describe our

lensing measurement methods in Section 3. In Section 4, we analyze the measured lensing signals and the corresponding dependence on central galaxy morphologies and the properties of the galaxy clusters. Subsequently, in Section 5, we explore the underlying physical origins using the SIMBA and TNG simulations. Finally, we summarize our findings in Section 6.

2. DATA

2.1. CMASS

We use the galaxy morphology catalog measured by Xu & Jing (2022), with the galaxy sample selected from Baryon Oscillation Spectroscopic Survey (BOSS, Ahn et al. (2012); Bolton et al. (2012)) constant-mass (CMASS), with an area of approximately 500 deg^2 overlapping with HSC. We select central galaxies with stellar masses in the narrow range of $11.3 < \log(M_*/\mathrm{M}_\odot) < 11.7$ and a redshift range of 0.45-0.7 as our lens sample. The Sérsic indices are obtained by fitting the Sérsic profile to the corresponding HSC z-band images, as detailed in Xu & Jing (2022). In this study, we focus on galaxies with Sérsic indices ranging from 0.8 to 8.

2.2. HSC

The shear catalog we use is processed through the Fourier_Quad (FQ; Zhang 2008) pipeline, based on the third public data release of HSC, which covers an area of about 1400 deg^2 and includes about 100 million galaxies (Liu et al. 2024). The FQ method employs multipole moments of galaxy images in Fourier space for shear measurements, including five shear estimators: G_1, G_2, N, U, and V. G_i is based on the galaxy quadrupole moments in Fourier space. N is a normalization factor used to estimate and correct the impact of noise and the Point Spread Function (PSF). U and V are the additional terms taking care of the parity properties of the shear estimators in the PDF-SYM method, which is a novel way of estimating shear statistics. Their specific definitions can be found in Zhang et al. (2016).

The shear catalog records basic information about galaxies such as position, signal-to-noise ratio (ν_F, Li & Zhang (2021)), magnitude, and shear estimators. Photometric redshift (photo-z) information is sourced from the DEmP method in Nishizawa et al. (2020), which demonstrates very low bias and scatter for photo-z less than 1.5. Therefore, we limit the maximum photo-z of background galaxies to 1.5. Additionally, in the lensing analysis, we ensure that the photo-z of background galaxies is larger than the lens redshift plus 0.1, i.e., $z_s > z_l + 0.1$. To enhance the accuracy of shear measurements, we select background galaxies with $\nu_F > 4$. HSC observes in five bands: g, r, i, z, and y, with the

i band offering the best imaging quality. In the FQ method, shear estimators are measured for each galaxy image without stacking images from different bands. According to Liu et al. (2024), we choose data from the r, i, and z bands as the shear sample, as their multiplicative shear bias in the field distortion tests is at about 1-2 percent level at most, and their galaxy-galaxy lensing measurements show consistency with the results from the HSC year-one official shear catalog.

More recently, it is found in Shen et al. (2024) that additional shear multiplicative bias can be induced by the photo-z cut of the background sample, which is a selection effect unknown before. We therefore find it necessary to calibrate for the multiplicative bias that may arise due to the selection of a subset of the background sample in the measurement of, e.g., galaxy-galaxy lensing. Fortunately, the FQ shear catalog keeps the field distortion information for each galaxy image/shear estimator, it therefore provides a convenient on-site calibration approach. Its details relevant to this work is provided in Appendix A.

2.3. *Simulations*

In our work, we study two hydrodynamic simulations, TNG and SIMBA, to compare our observational results and explore the origins of various relationships. TNG is a series of large cosmological gravity-magnetohydrodynamics simulations that incorporate comprehensive models of galaxy formation physics (Pillepich et al. 2017). We utilize the simulation with a box length of $L_{\mathrm{box}} = 205\mathrm{Mpc}/h$, denoted as TNG300. The SIMBA simulation provides detailed modeling of black hole growth and feedback, successfully reproducing many observational results (Davé et al. 2019; Thomas et al. 2019; Cui et al. 2021). Specifically, AGN feedback in SIMBA operates in three modes based on the accretion rate: the radiative mode at high Eddington ratios f_{Edd}, and the jet and X-ray modes at low f_{Edd}. For our primary analysis, we use the full physics simulation with $L_{\mathrm{box}} = 100\,\mathrm{Mpc}/h$, denoted as S100. According to Weinberger et al. (2018); Davé et al. (2019); Rodríguez Montero et al. (2019), kinetic feedback modes are primarily responsible for quenching massive central galaxies in both SIMBA and TNG, while major galaxy mergers are not the main drivers of most quenching events. Thus, we also utilize various AGN feedback simulations from SIMBA with $L_{\mathrm{box}} = 50\,\mathrm{Mpc}/h$ (S50) to study their effects.

We first select central galaxies with stellar masses in the range of $11.3 < \log M_*/\mathrm{M}_\odot < 11.7$ from TNG300 and S100 to match the observation, and then choose the range $11 < \log M_*/\mathrm{M}_\odot < 11.5$ for S50 series simula-

tions due to their limited volume. The stellar mass is defined as the sum of the masses of stars within twice the stellar half-mass radius. Assuming a constant mass-to-light ratio, we create galaxy images for each galaxy's stellar mass distribution, extending to 4×4 times the half-stellar mass radius. Then we convolve a small gaussian PSF to reduce noises. We fit these images with a 2D Sérsic profile to obtain their Sérsic index n. Additionally, we fit the surface density of the host halos with an NFW profile to obtain their halo mass M_h and concentration c. The definitions in NFW model are aligned with our lensing measurements. We use the position with the minimum gravitational potential energy as the real center of halos, hence the off-centering effect can be ignored in this part. Finally, since there is a slight correlation between n and M_*, we resample the stellar mass distribution of galaxies with different n to make their distributions similar, in order to eliminate the impact of stellar mass on the results.

3. MEASUREMENT

3.1. *PDF-SYM for ESD*

Galaxy-galaxy lensing measures the correlation between the position of an object and the surrounding shear, which can reflect the excess surface density (ESD) around the object. For a spherically symmetric lensing potential, the relationship between shear and ESD is given by

$$\Delta\Sigma(R) = \overline{\Sigma}(< R) - \Sigma(R) = \Sigma_c \gamma_t(R), \qquad (2)$$

where $\overline{\Sigma}_0(< r)$ refers to the average surface density within a radius r. Σ_c is the comoving critical surface density, defined as

$$\Sigma_c = \frac{c^2}{4\pi G} \frac{D_{\mathrm{s}}}{D_{\mathrm{l}} D_{\mathrm{ls}} (1 + z_{\mathrm{l}})^2} \qquad (3)$$

Here, c is the speed of light, G is the gravitational constant, and D_{s}, D_{l}, and D_{ls} are the angular diameter distances for the lens, source, and lens-source systems, respectively.

In our work, we employ the PDF-symmetrization (PDF-SYM, Zhang et al. (2016)) method to measure the ESD of galaxies. The essence of this method lies in constructing the Probability Density Function (PDF) of the shear estimators, and adjusting the assumed underlying shear value to achieve the most symmetric state of the PDF, thereby obtaining the optimal shear estimate. For the ESD signal at a given radius r, we can obtain the PDF of the shear estimators $P(G_t)$ for the background galaxies. By hypothesizing an ESD signal $\widehat{\Delta\Sigma}$, we adjust $P(G_t)$ to $P(\hat{G}_t)$ by modifying each value

of G_t via:

$$\hat{G}_t = G_t - \frac{\widehat{\Delta\Sigma}}{\Sigma_c}\left(N \pm U_t\right). \tag{4}$$

When $\widehat{\Delta\Sigma}$ equals the true ESD signal, the new distribution $P(\hat{G}_t)$ will achieve the most symmetric state.

In this study, we uniformly divide the radius range from 0.05 to 20 Mpc/h into 8 bins in logarithmic space for measurement and estimate the covariance matrix by dividing the sky into 86 sub-regions using Jackknife method. Additionally, to remove the effects of boundary from the observed region and some systematic bias, we subtract the signal contribution from random points, the number of which is 10 times the number of lens galaxies. Additionally, we correct the multiplicative biases introduced in shear measurements and details are shown in Appendix A.

3.2. Modeling and Fitting

For the ESD model, we take into account the effects of stellar mass of galaxies, individual halos, off-centering effects, and the 2-halo term. The mass of the galaxy primarily affects the ESD at small radii, typically regarding the central galaxy as a point source and

$$\Delta\Sigma_*(R) = \frac{M_*}{\pi R^2} \tag{5}$$

where M_* is the stellar mass of central galaxy, as shown in Table 1 for all subsamples. We adopt NFW model (Navarro et al. 1997) to describe an individual halo profile, whose density is expressed as

$$\rho(r) = \frac{\rho_0}{(r/r_s)(1+r/r_s)^2} \tag{6}$$

with $\rho_0 = \rho_m \Delta_{\rm vir}/(3I)$, where $I = [\ln(1+c) - c/(1+c)]/c^3$. $r_{\rm vir}$ is the virial radius, r_s is the scale radius and the concentration c of halos is defined by $c = r_{\rm vir}/r_s$. In this paper, we define a halo as a sphere with an overdensity of $\Delta_{\rm vir} = 180$ times the mean matter density ρ_m, with a halo mass $M_h = 180(4\pi/3)\rho_m r_{\rm vir}^3$. The unit of M_h in this paper is $M_\odot/h$. We employ the analytical expression for the surface density $\Delta\Sigma_{\rm NFW}$ as presented in Yang et al. (2006).

The off-centering effect is a significant consideration within the virial radius of halos, as it can lead to an underestimation of the ESD signal at smaller radii. Ignoring this effect might result in an underestimation of the halo's mass and concentration. Thus, the 1-halo term ESD model typically divides the halo profile into well-centered and off-centered components,

$$\Delta\Sigma_{\rm 1h}(R) = f_c \Delta\Sigma_{\rm NFW}(R) + (1-f_c)\Delta\Sigma_{\rm off}(R) \tag{7}$$

where f_c is the proportion of well-centered halos. $\Sigma_{\rm off}$ refers to mean surface density of mis-centered halos, which can be derived from

$$\Sigma_{\rm off}(R) = \frac{1}{2\pi}\int_0^\infty dR_{\rm off} P(R_{\rm off}) \int_0^{2\pi} d\theta$$
$$\times \Sigma_{\rm NFW}\left(\sqrt{R^2 + R_{\rm off}^2 + 2RR_{\rm off}\cos\theta}\right). \tag{8}$$

where $P(R_{\rm off})$ is the distribution of offset centers on radius and it is generally assumed to be Rayleigh distribution (Johnston et al. 2007)

$$P(R_{\rm off}) = \frac{R_{\rm off}}{\sigma_s^2}\exp\left(-\frac{R_{\rm off}^2}{2\sigma_s^2}\right) \tag{9}$$

Given that our measurement radii significantly exceed the common virial radii of halos, the 2-halo term exerts a substantial influence on the ESD. According to Yang et al. (2006), the surface density of the 2-halo term is correlated with the galaxy-matter cross-correlation,

$$\Sigma_{\rm 2h}(R) = 2\rho_m \int_R^\infty [1 + \xi_{\rm gm}(r)]\frac{r\,dr}{\sqrt{r^2 - R^2}} \tag{10}$$

where $\xi_{\rm gm}(r) = b_h(M_h, z)\xi_{\rm mm}(r)$. $b_h(M_h, z)$ is the halo bias, which is modeled by Tinker et al. (2010). $\xi_{\rm mm}(r)$ is calculated by COLOSSUS (Diemer 2018) using a semi-analytical power spectrum from Eisenstein & Hu (1998). Finally, our ESD model can be summerized as

$$\Delta\Sigma(R) = \Delta\Sigma_*(R) + \Delta\Sigma_{\rm 1h}(R|M_h, c, \sigma_s, f_c) + \Delta\Sigma_{\rm 2h}(R|M_h) \tag{11}$$

To enhance the accuracy of our model, we divide the redshift range of 0.45 to 0.7 into five bins and perform an integration based on the distribution of lens galaxies. Our model comprises four free parameters, halo mass M_h, concentration c, the scatter of off-centering σ_s and the proportion of well-centered halos f_c, which we fit using Markov Chain Monte Carlo techniques (Christensen & Meyer 2000).

4. RESULTS AND DISCUSSION

4.1. Halo mass dependence on galaxy Sérsic index and color

We divide the galaxy samples with stellar masses in the range of $11.3 < \log M_*/M_\odot < 11.7$ into five subsamples. The range of their Sérsic indices n, the number of galaxies, and the average stellar mass are presented in Table 1. Figure 1 shows the measurements of ESD, with their corresponding best-fit curves and the different components of the model. It is evident that the ESD increases with higher n. The "All" section in Table 1 presents the fitting results for all parameters. To
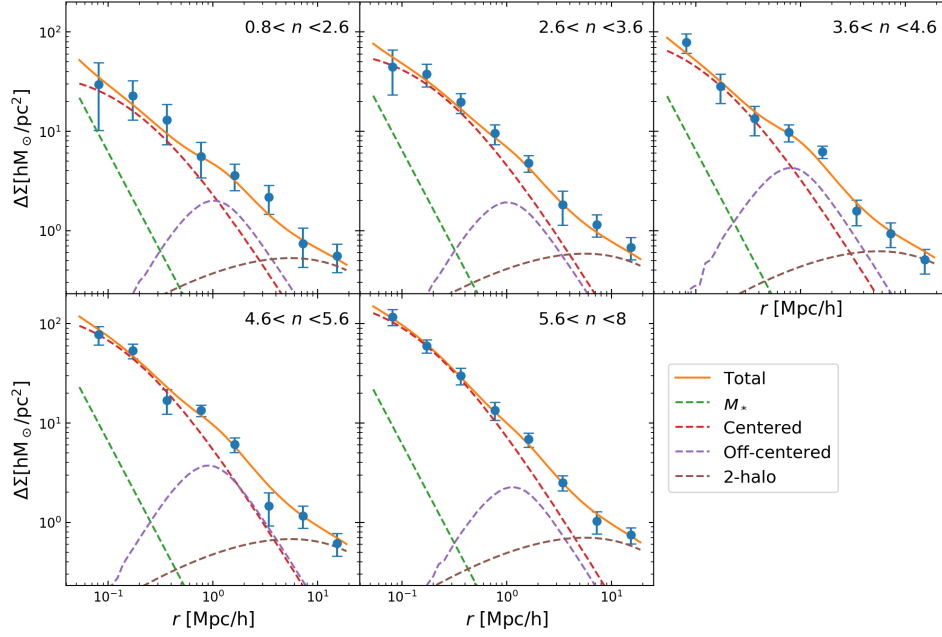
Figure 1. Measurement of the lensing ESD around central galaxies with different Sérsic indices n. Solid lines represent the best-fit curves, and dashed lines represent ESD of different components, including stellar mass, well-centered portion, off-centered portion and 2-halo term.
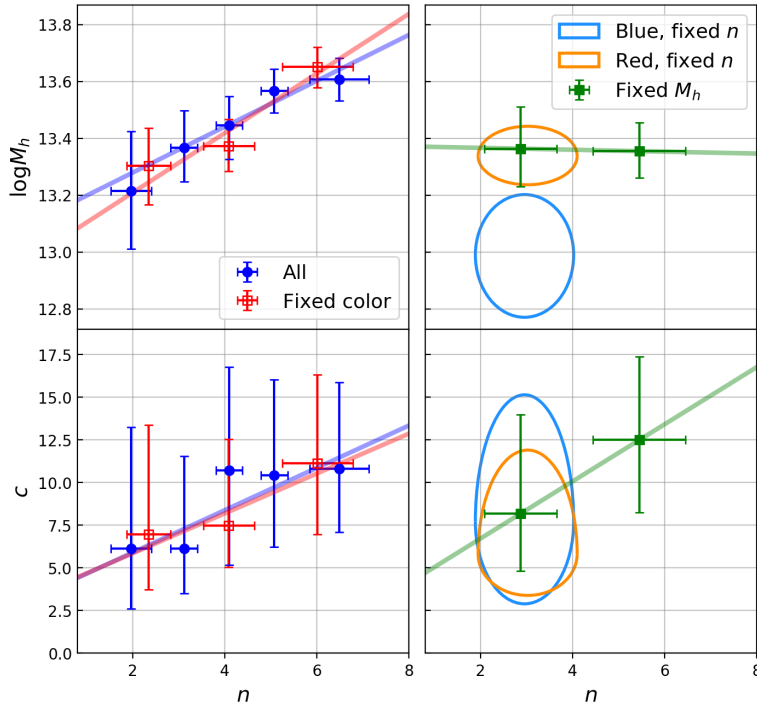

Figure 2. Best-fit halo mass $\log M_h$ and concentration c under different conditions. Blue dots represent all samples with different Sérsic indices n, and red dots represent results for different n with fixed sample color. Light blue and orange rings represent results for blue and red galaxies, respectively, while fixed n, with ring size representing the 1σ range.

clearly show the trend of the parameters, we depict the relationship between halo mass M_h and halo concentration c as blue dots in Figure 2, with the horizontal axis representing the average n for each sample. We find that halo mass increases significantly with the increase of the Sérsic index, which is consistent with the conclu-

Table 1. Fitting results for halo mass $\log M_h$, concentration c, scatter in off-centering σ_s, and the proportion of well-centered galaxies f_c in all subsamples. "All" refers to samples controlled only by constant stellar mass. "Fixed color" refers to samples where galaxy color is also controlled, and "Fixed n" refers to samples controlled by Sérsic index. "Fixed M_h" is to control the the halo mass of subsamples by applying the selection on M_G, where M_G is the halo mass assigned by abundance matching in group catalog Yang et al. (2021). Middle panel shows conditions of subsamples and the information, including the number of galaxies N_{lens} and their average stellar mass $\log M_*/\mathrm{M}_\odot$.

Samples	n / color	N_{lens}	$\log M_*$	$\log M_h$	c	σ_s	f_c	χ^2/ν
	$0.8 < n < 2.6$	1453	11.46	$13.22^{+0.21}_{-0.20}$	$6.14^{+7.11}_{-3.53}$	$0.76^{+0.28}_{-0.36}$	$0.37^{+0.33}_{-0.18}$	0.60
	$2.6 < n < 3.6$	1744	11.48	$13.37^{+0.13}_{-0.12}$	$6.13^{+5.43}_{-2.62}$	$0.67^{+0.35}_{-0.36}$	$0.55^{+0.26}_{-0.22}$	0.37
All	$3.6 < n < 4.6$	1985	11.48	$13.45^{+0.10}_{-0.12}$	$10.72^{+6.05}_{-5.53}$	$0.51^{+0.18}_{-0.12}$	$0.35^{+0.26}_{-0.11}$	1.86
	$4.6 < n < 5.6$	1883	11.48	$13.57^{+0.08}_{-0.08}$	$10.42^{+5.60}_{-4.20}$	$0.53^{+0.26}_{-0.14}$	$0.46^{+0.23}_{-0.13}$	1.25
	$5.6 < n < 8$	1783	11.46	$13.61^{+0.08}_{-0.07}$	$10.81^{+5.07}_{-3.71}$	$0.65^{+0.31}_{-0.28}$	$0.57^{+0.21}_{-0.14}$	0.34
Fixed color	$0.8 < n < 3$	826	11.50	$13.30^{+0.13}_{-0.14}$	$6.97^{+6.42}_{-3.23}$	$0.42^{+0.47}_{-0.22}$	$0.52^{+0.31}_{-0.27}$	0.34
$(2.3 < u - r < 2.7)$	$3 < n < 5$	2560	11.49	$13.37^{+0.09}_{-0.09}$	$7.48^{+5.07}_{-2.42}$	$0.55^{+0.32}_{-0.23}$	$0.63^{+0.23}_{-0.21}$	2.08
	$5 < n < 8$	2102	11.47	$13.65^{+0.07}_{-0.07}$	$11.15^{+5.17}_{-4.17}$	$0.59^{+0.29}_{-0.18}$	$0.46^{+0.22}_{-0.12}$	0.49
Fixed n	$2 < u - r < 2.25$	1195	11.42	$12.99^{+0.21}_{-0.22}$	$7.72^{+7.43}_{-4.82}$	$0.67^{+0.33}_{-0.30}$	$0.38^{+0.34}_{-0.22}$	1.05
$(1 < n < 6)$	$2.25 < u - r < 2.6$	1202	11.43	$13.34^{+0.10}_{-0.10}$	$5.81^{+6.10}_{-2.42}$	$0.20^{+0.59}_{-0.07}$	$0.35^{+0.43}_{-0.23}$	1.31
Fixed M_h	$0.8 < n < 4$	1361	11.49	$13.36^{+0.15}_{-0.13}$	$8.19^{+5.80}_{-3.36}$	$0.78^{+0.30}_{-0.46}$	$0.55^{+0.26}_{-0.20}$	1.27
$(13.3 < \log M_G < 13.8)$	$4 < n < 8$	1923	11.49	$13.36^{+0.10}_{-0.09}$	$12.50^{+4.87}_{-4.26}$	$0.54^{+0.34}_{-0.22}$	$0.61^{+0.22}_{-0.16}$	1.30

sions from Xu & Jing (2022). Additionally, we observe a possible evidence that more concentrated galaxies (high n) may reside in more concentrated halos (high c), although the uncertainties are relatively large with current data. We fit the blue dots in the figure using linear relationships , yielding:

$$\log M_h = 0.08^{+0.03}_{-0.03} n + 13.13^{+0.17}_{-0.17} \quad \text{[All]}, \qquad (12)$$

$$c = 1.0^{+1.3}_{-1.4} n + 5.3^{+6.9}_{-5.7} \quad \text{[All]}. \qquad (13)$$

In terms of galaxy properties, higher Sérsic indices are typically associated with early type galaxies with red colors, while lower Sérsic indices refer to late type galaxies with blue colors (see, e.g., Figure 1 of Xu & Jing 2022). It has long been recognized that red and blue galaxies exhibit distinct SHMR (e.g. More et al. 2011; Peng et al. 2012; Wang & White 2012; Rodríguez-Puebla et al. 2015; Mandelbaum et al. 2016; Wang et al. 2021; Posti & Fall 2021; Xu & Jing 2022; Alonso et al. 2023), with red galaxies hosted by more massive dark matter halos than blue ones at fixed stellar mass. Given the strong correlation between morphology and color, it is crucial to determine which of these secondary dependencies is more fundamental. Does the halo mass dependence on n arise due to color, or is it the other way around?

Therefore, we select galaxies with rest-frame $u - r$ colors in a narrow range of 2.3 to 2.7. We divide them into three subsamples according to the Sérsic index, n,

and resample their color distributions to be the same to eliminate the correlation between color and n. The left panel of Figure 3 shows their ESD measurements. The red empty squares with errorbars in Figure 2 show the best-fit M_h and c versus n, and the "Fixed color" row in Table 1 presents the best-fit parameters and associated errors. We find that after the color is fixed, the dependencies of both M_h and c on n are still consistent with the results of the blue dots. The best-fit relations are

$$\log M_h = 0.11^{+0.04}_{-0.04} n + 12.99^{+0.20}_{-0.19} \quad \text{[Fixed color]}, \quad (14)$$

$$c = 0.8^{+1.7}_{-1.8} n + 6.3^{+8.4}_{-7.0} \quad \text{[Fixed color]}, \qquad (15)$$

This implies that the correlation between n and halo properties is not predominantly driven by differences in galaxy color. Conversely, to explore whether the color dependence is driven by morphology, we also select galaxies with $1 < n < 6$ and divide them into two color subsamples: blue galaxies with $2 < u - r < 2.25$ and red galaxies with $2.25 < u - r < 2.6$. For fair comparison, these two sub-samples are resampled to have the same distribution of n, with average n of 2.98 ± 1.07 and 3.10 ± 1.09, respectively. The middle panel of Figure 3 shows their ESD measurements. The orange and blue rings in Figure 2 represent the results for the red and blue galaxy samples, with their sizes indicating the 1σ error range. The "Fixed n" section in Table 1 shows the best-fit results. We find that even when n is fixed, halo mass still exhibits a color bimodality, with red galaxies residing in more massive halos than blue galaxies,
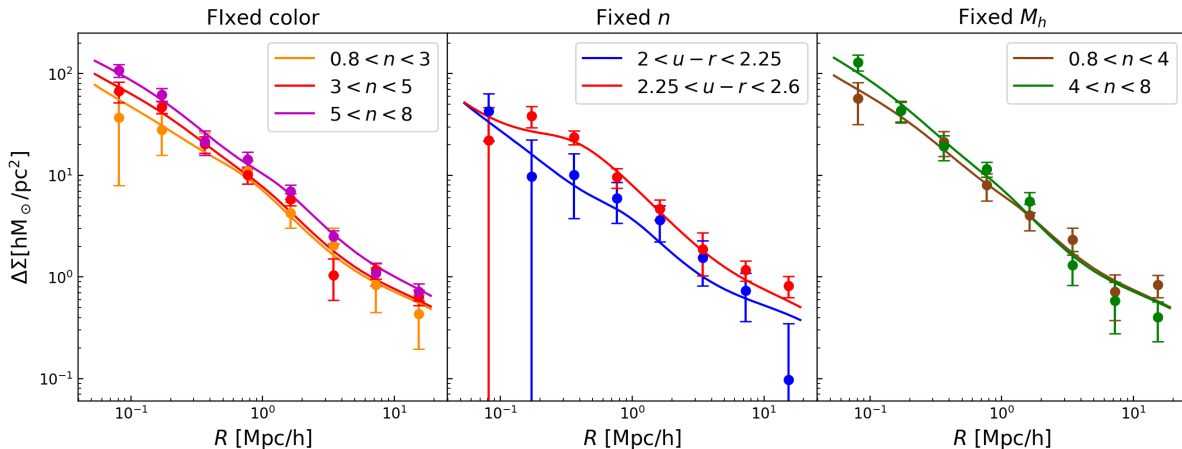
Figure 3. Dots with errorbars are measured lensing ESD signals. Solid lines are the best fits. In the left, middle and right panels, galaxies are grouped according to their Sérsic indices at fixed color, by color at fixed Sérsic index and by Sérsic indices at fixed host halo mass obtained through abundance matching. These are indicated by different colors (see the legend).

while their halo concentrations remain consistent. This suggests that a better secondary proxy for halo mass should involve a combination of both color and morphology. Due to data limitations, we are unable to determine the optimal combination, but this presents an intriguing topic for future research. On the other hand, halo concentration appears to be primarily linked to morphology, although more precise measurements are needed to confirm this conclusion.

4.2. Halo mass dependence on group richness or satellite distribution

Galaxy properties and evolution are typically shaped by their surrounding environment, including local matter density and the evolutionary history of their host halos. We further investigate the properties of galaxy groups hosting the central galaxies using the group catalog from Yang et al. (2021), which provides details on group richness and member galaxies.

The left panel of Figure 4 shows the richness distributions of groups with different n of central galaxies in our sample. The vertical dashed lines indicate the mean richness for each sample. We find that central galaxies with larger n are more likely to be located in groups with higher richness. Also, we calculate the projected number density profiles of satellite galaxies at various projected radii, displayed in the right panel of Figure 4. It shows that the surrounding density of companion satellite galaxies increases with the n of central galaxies, consistent with the results from Xu & Jing (2022). In fact, many previous studies have pointed out the tight correlation between the host halo mass and cluster richness or satellite abundance (e.g. Rozo et al. 2009; Andreon & Hurn 2010; Wang & White 2012; Simet et al. 2017; Murata et al. 2018, 2019; Phriksee et al. 2020;

Chiu et al. 2020; Wang et al. 2021; Tinker et al. 2021; Chen et al. 2024), and thus our results here are related to the fact that galaxies with larger Sérsic indices are hosted by more massive dark matter halos.

4.3. Interpretations on the correlation between halo concentration and galaxy Sérsic index

In Figure 2, we find evidence of a positive correlation between the Sérsic index and halo concentration. A similar pattern is observed in the satellite distribution in Figure 4. While more precise measurements are needed to fully confirm this relation, it would be intriguing to explore its theoretical implications.

It is generally believed that more massive halos form later and have lower concentrations (e.g. Maccio et al. 2007; Duffy et al. 2008; Mandelbaum et al. 2008; Correa et al. 2015; Ludlow et al. 2014, 2016), as material continues to flow in from outer regions (e.g. Fong & Han 2021; Gao et al. 2023; Diemer 2022; He et al. 2024). However, in our results, we find that both the host halo mass and halo concentration are positively correlated with the Sérsic index of galaxies (showing positive $n - M_h$ and $n - c$ relations). If the $n - c$ relation were solely driven by the negative halo mass-concentration relation for dark matter halos, we would expect a negative $n - c$ relation instead. Therefore, the positive correlation we observe between halo concentration and the Sérsic index is likely driven by more intrinsic factors beyond the typical mass-concentration relation of dark matter halos.

Navarro et al. (1997) propose that older halos, which formed in higher cosmic densities, tend to have larger characteristic densities and concentrations. Using high-resolution N-body simulations, Zhao et al. (2009) find that the halo concentration is tightly correlated with the universe age when its progenitor first reaches 4% of their
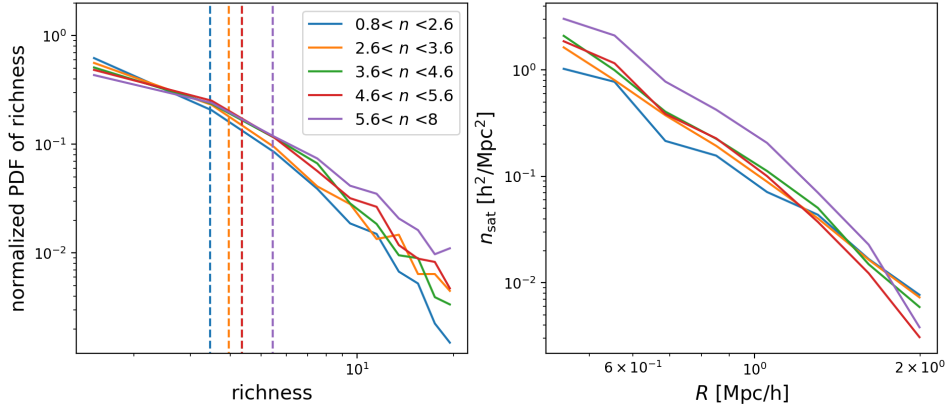
Figure 4. The left panel shows the normalized richness distribution of galaxy clusters with different galaxy Sérsic indices, where dashed lines represent the average richness of each subsample. The right panel displays the projected number density profiles of companion galaxies as a function of projected radius.

current mass, i.e. $t/t_{0.04}$ in their work. Therefore, we speculate that two main factors may influence the $n - c$ relation in our results. One is introduced by the halo mass-concentration relation, that the positive $n - M_h$ relation would introduce negative correlations between n and c. The other is that more concentrated galaxies with larger Sérsic indices form earlier at fixed stellar mass, with their host halos form earlier as well, and dark matter halos with earlier formation times have larger concentrations. Among these two factors, the latter may play a dominant role for our galaxy samples.

To further test our hypothesis, we control halo mass in the sample by using the halo mass from the group catalog M_G, which is assigned using the abundance matching technique (Yang et al. 2021). We select galaxies with $10^{13.3} < M_G < 10^{13.8} \mathrm{M}_\odot/h$ and divide them into two subsamples based on their Sérsic index (n) to measure the ESD. The right panel of Figure 3 shows the ESD measurements, Table 1 presents sample information and best-fit parameters , which are also shown by the green square points in Figure 2. We find that the halo masses from the group catalog of the two subsamples are very consistent, but halo concentrations for galaxies with larger Sérsic indices are higher, still consistent with the $n - c$ relation shown and discussed earlier. Furthermore, compared to the $n - c$ relation without controlling halo mass, the relation becomes steeper. This implies that by reducing the negative $M_h - c$ relationship caused by accretion and merging, the positive correlation between n and c becomes slightly strengthened. This also supports our speculation that the host halos of galaxies with higher Sérsic indices are formed earlier, leading to higher halo concentrations, and this effect is stronger than the influence of later-time halo mergers to decrease the concentration at least for the massive CMASS galaxies at $z \sim 0.57$.

4.4. Comparison with other results
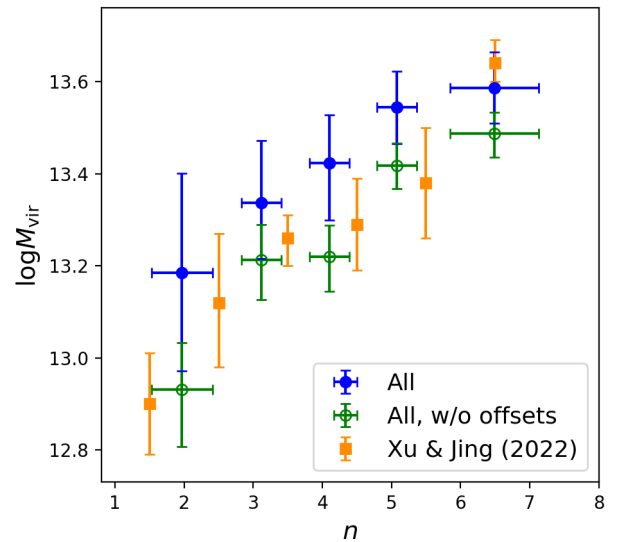
Figure 5. The relationships between n and halo mass measured in different ways. The definition of halo mass M_{vir} here is from Bryan & Norman (1998). Blue dots represent our results for all samples. Green hollow points indicate the results obtained without considering off-centering effects in the halo model. Orange square dots display the results from Xu & Jing (2022).

Figure 5 compares our main results (blue dots) with those obtained using the PAC method in the work of Xu & Jing (2022) (orange squares). To ensure a consistent basis for comparison, we convert the halo masses in our results to their definition, where $\Delta_{\mathrm{vir}} = 18\pi^2 + 82x - 39x^2$ and $x = \Omega_m(z) - 1$. We observe that our results systematically yield higher halo masses. This discrepancy may stem from the assumption in Xu & Jing (2022) that massive central galaxies are perfectly sit-

uated at the halo centers, neglecting the off-centering effects in observations. By setting $f_c = 1$ in our model, disregarding the central offsets, we show the fitting results as green hollow points in the figure. In this test, our results align well with theirs.

5. COMPARISON WITH SIMULATIONS

So far we have probed how do the host halo properties correlate with galaxy and galaxy cluster properties. However, the physical drivers behind these relationships are still under debates. Cui et al. (2021) quantitatively reproduce the color bimodality of the SHMR in the SIMBA simulations (Davé et al. 2019), showing that red galaxies reside in more massive halos at a given stellar mass. They find that this is mainly due to active galactic nuclei (AGN) feedback in the form of jets and X-rays, which significantly suppresses star formation earlier in red galaxies while their halos continue to grow. This also could be the reason of the $n - M_h$ relationship. Therefore, we further investigate similar relations in this section, using two hydrodynamic simulations, TNG and SIMBA.

5.1. *The relationship between Sérsic index and halo properties*

Before proceeding, we need to clarify some problems when measuring the galaxy morphology in SIMBA: the galaxies in these simulations generally exhibit very low galaxy concentrations, with n not exceeding 2. According to Davé et al. (2019), the size of low-mass quenched galaxies in SIMBA is a notable failure of the current model, as their half-light radii are larger than those of star-forming galaxies, which contradicts observational trends. A larger radius usually implies a lower concentration, leading to elliptical galaxies that should have higher n but obtaining very low n values in the simulation. Nevertheless, we endeavor to incorporate the results from SIMBA in our analysis within the limited range of n it produces.

Firstly, we use snapshots from TNG300 and SIMBA at two redshifts for the main analysis, $z = 0$ and $z = 0.55$ respectively[1]. Figure 6 displays the relationships between the Sérsic index, n, and the halo mass, M_h, halo concentration, c, and richness, λ, for central galaxies in simulations. The properties of galaxies and halos are represented by scatter plots, with the linear fits represented by lines, and the 16-84 percentiles displayed as shaded areas. Regarding the relationship between halo mass and n, we find that both TNG300 and

SIMBA exhibit correlations, even though the correlation in TNG300 is weaker than our observational results (Eq.12). While the S100 simulation shows a stronger correlation, considering its incorrect galaxy morphology, we only qualitatively analyze the trends. Both simulations demonstrate a positive correlation between n and halo abundance λ, which is qualitatively consistent with our results (Figure 4). Moreover, we note that the correlations between n and other galaxy and halo properties at higher redshift are weaker than those at lower redshift.

However, neither of the two simulations reproduce significant positive correlations between halo concentration and n as have been observed in the real data. A strong negative correlation even shows in SIMBA. As previously discussed, the $n - c$ relation at fixed stellar mass is affected by: 1) the mass-concentration ($M_h - c$) relation of dark matter halos; and 2) the intrinsic $n - c$ relation at fixed halo mass. To validate our idea that more concentrated galaxies are hosted by more concentrated halos, we control both halo mass and stellar mass in a subsample from the TNG300 at $z = 0$. The left panel of Figure 7 shows the correlation between halo mass and stellar mass for the red points in Figure 6, color coded by n. We select galaxies within the red box in the panel and replot the correlations between n and other properties for them in right panels of Figure 7. We find that after controlling both the stellar mass and halo mass to a narrow range, the halo concentration shows a slight positive correlation with n. This might imply that, for central galaxies with the same stellar mass and halo mass, more concentrated central galaxies are more likely to reside in more concentrated halos, which is consistent with our previous hypothesis and results. However, the correlation is still weak and may depend on the details of galaxy formation models adopted in the simulations and how realistic are these models.

5.2. *The effects of AGN feedback in SIMBA*

We further examine the relationship between n and the black hole (BH) mass $M_{\rm BH}$ in the galaxies for the two simulations at $z = 0$, as shown in Figure 8. We find a weak positive correlation between n and $M_{\rm BH}$ in both TNG300 and S100. We consider this to be natural because a larger n typically implies that a galaxy has a more dominant bulge component, and many studies reported a positive correlation between bulge and black hole mass (McLure & Dunlop 2002; Wandel 2002; McConnell & Ma 2013; Davis et al. 2019). We also display the relationship between $M_{\rm BH}$ and M_h, revealing strong positive correlations. We can derive the relationship between $\log M_h$ and n by combining the best-fit equations

---

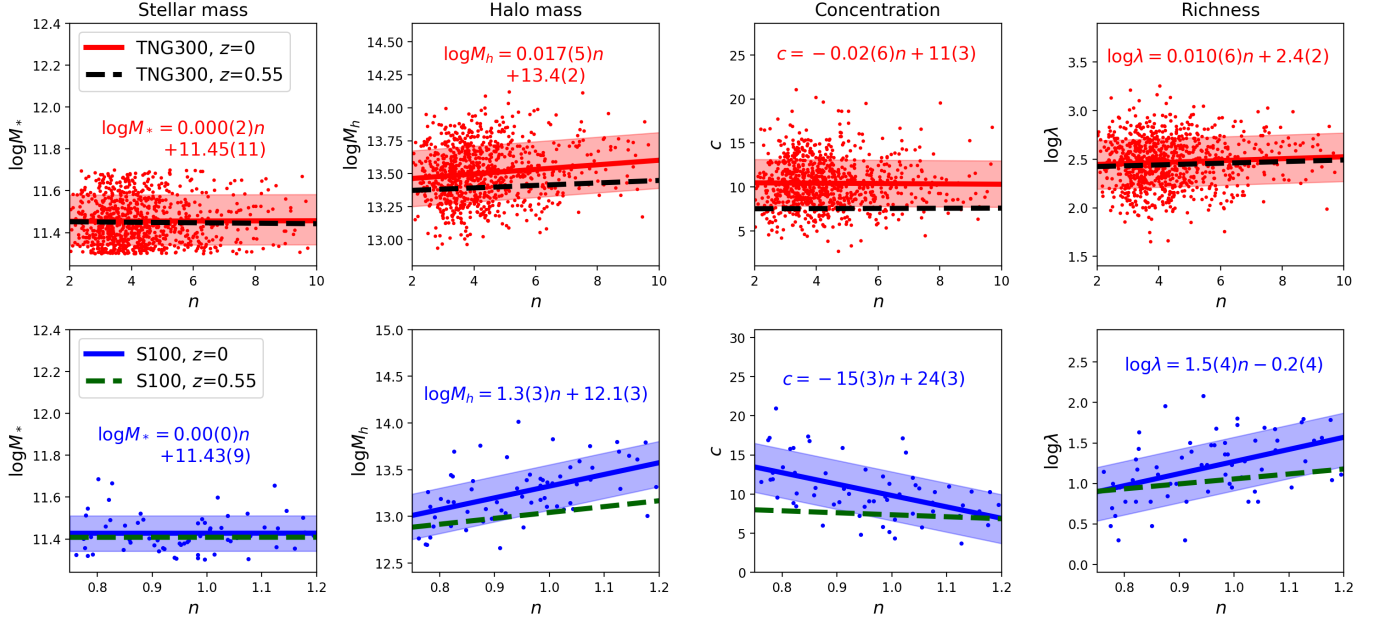[1] The latter is actually $z = 0.556839$ for SIMBA, but denoted as 0.55.

Figure 6. The correlations between the Sérsic index (n) of central galaxies and their host halo mass, halo concentration, and richness in two simulations, S100 and TNG300. Central galaxies are selected to have stellar masses in the range of $11.3 < \log M_*/\mathrm{M_\odot} < 11.7$ for snapshots at redshift of 0 and 0.55. Solid lines represent linear best-fit results for samples at $z = 0$ (dots), with shaded areas indicating the 16th to 84th percentiles. While dash lines represent the fitting results for samples at $z = 0.55$. The formula provided in each panel gives the best-fit result to galaxy systems at $z = 0$, in which the numbers in the parentheses represent the 1σ errors of the last digit or last two digits.
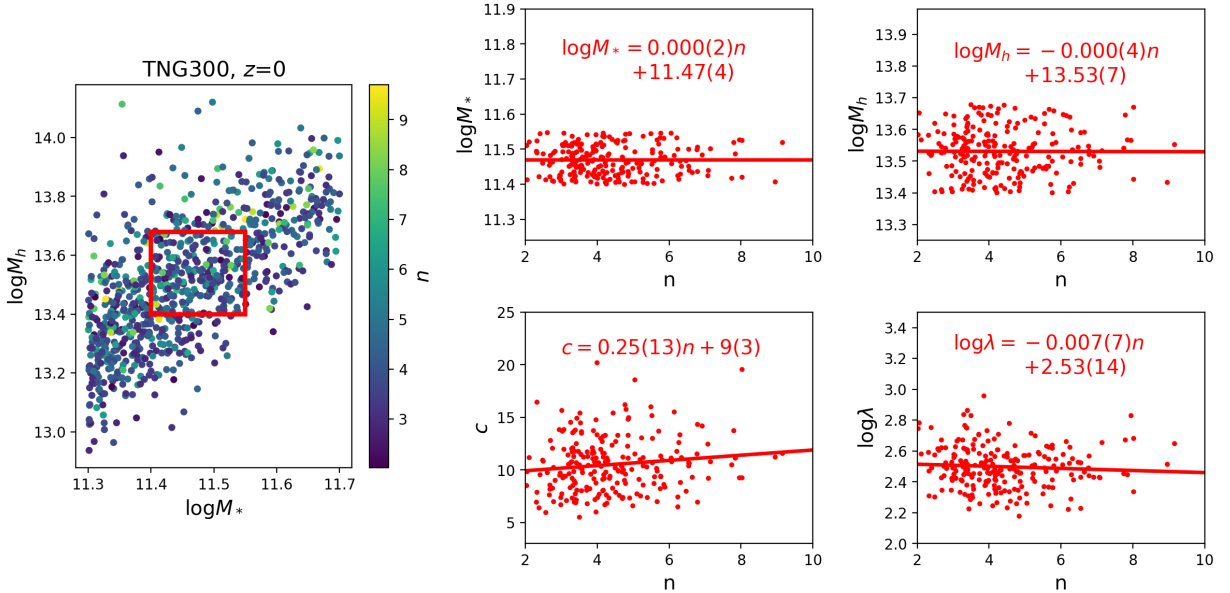
Figure 7. The left panel shows halo mass (M_h) as a function of stellar mass (M_*) for samples in the TNG300 simulation at $z = 0$ (red dots in Figure 6), colour-coded by their Sérsic indices, n. We select the subsample within the red box to simultaneously control both M_* and M_h. The right panel displays the dependencies of the Sérsic index, n, on stellar mass, halo mass, halo concentration, and richness for this subsample.

in $\log M_{\mathrm{BH}} - n$ and $\log M_{\mathrm{BH}} - \log M_h$ panels, and we find that the results are consistent with those obtained from the direct fitting shown in Figure 6. This implies

that the correlation between the Sérsic index and halo mass is probably derived from the different black hole activities.
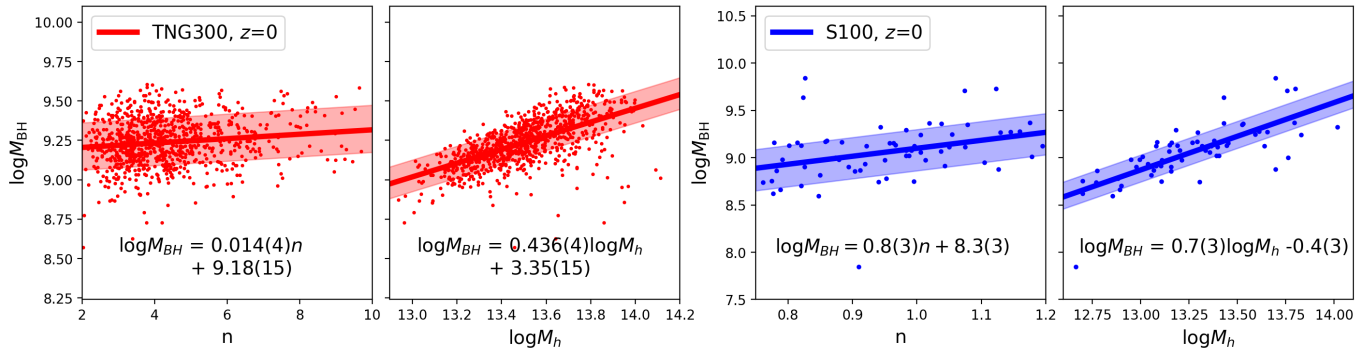
Figure 8. The relationship among n, black hole mass M_{BH} and halo mass M_h for galaxies from S100 and TNG300 at $z = 0$ (corresponding to the red and blue dots in Figure 6). The solid lines represent linear best-fit results and shaded areas represent the 16th to 84th percentiles, and the formulas in panels are equations of the solid lines.
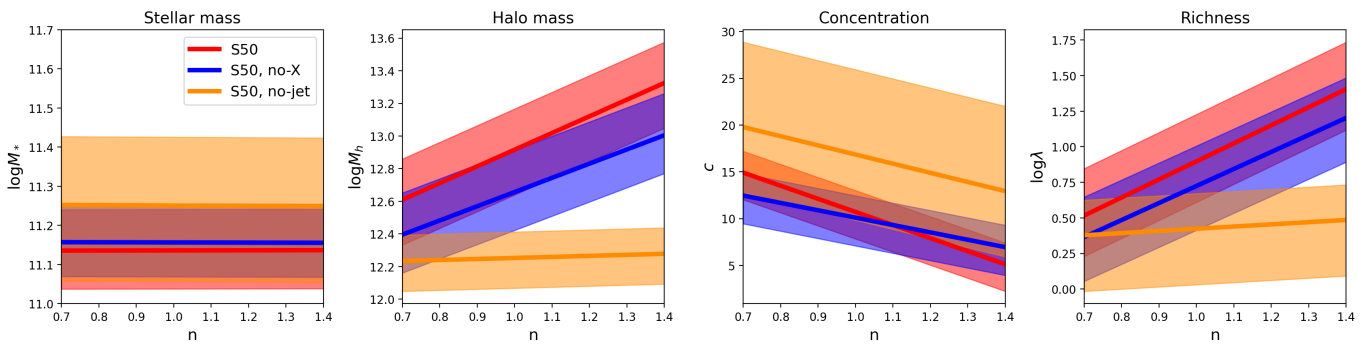
Figure 9. Similar to Figure 6, but the results are from three different simulations. "S50" represents the SIMBA simulation with a box length of 50 Mpc/h. "no-X" indicates a simulation without X-ray feedback, and "no-jet" represents a simulation without X-ray and jet mode AGN feedback.

According to Thomas et al. (2019), the Eddington ratio, f_{Edd}, of black holes is inversely correlated with their mass. When $f_{\mathrm{Edd}} < 0.2$, it would trigger jet-mode AGN feedback and subsequent X-ray AGN feedback. Therefore, to validate the $n - M_h$ relationship influenced by black hole mass, we use simulations from the SIMBA series with different modes of AGN feedback, including simulations that incorporate all physical processes ("S50"), that exclude X-ray feedback ("S50, no-X"), and that exclude both X-ray feedback and jet-mode AGN feedback ("S50, no-jet"). Figure 9 shows the correlations between n of central galaxies and other halo properties for three simulations, where the shaded regions represent the 16-84 percentiles. We observe distinctly different trends of n with other properties in the three simulations. As shown in the leftmost panel, the average stellar mass of galaxies without X-ray and jet-mode AGN feedback (orange) is higher than those with jet-mode AGN feedback (red and blue). This indicates that jet-mode feedback primarily reduces the star formation rate in galaxies, as stated in Davé et al. (2019). Furthermore, as AGN feedback modes are progressively turned off, the slope between halo mass and n gradually decreases. Es-

pecially in the "S50, no-jet" simulation, the correlation between n and M_h almost disappears, and the correlations with c and λ are also significantly weakened. These results indicate that the relationship between n and halo properties might be strongly influenced by the strength of AGN feedback, especially the jet mode, which can rapidly and effectively expel gas from galaxies, leading to the cessation of star formation.

6. SUMMARY AND CONCLUSION

We delve into the relationship between the morphology of central galaxies indicated by Sérsic index, n, and the properties of their host dark matter halos and galaxy groups/clusters, including halo mass, halo concentration and group richness. Our study in this paper extends the work of Xu & Jing (2022), in which the morphology, color, and size dependencies of the SHMR for massive central galaxies have been investigated using the PAC method. We use the central galaxy sample from their work, with a mass range of $11.3 < \log(M_*/\mathrm{M_\odot}) < 11.7$ and a redshift range of $0.45 - 0.7$, selected from BOSS CMASS observations. We employ galaxy-galaxy lensing to measure the ESD around these galaxies, using

the Fourier_Quad shear catalog from the third public data release of HSC. In our modeling approach, halo mass M_h and concentration c from the NFW profile were considered as free parameters, while also incorporating off-centering effects and 2-halo terms. We find the following:

- From lensing measurements, we discover a strong positive correlation between halo mass and the Sérsic index n of central galaxies with fixed stellar mass, demonstrating that more concentrated central galaxies are ensconced within more massive halos.

- To investigate whether galaxy Sérsic index, n, or galaxy color is a more fundamental secondary properties in determining halo mass, we separately control n and color for galaxies to be in a narrow range. The dependence of halo mass on both n and galaxy color still exists, which might indicate that some combinations of color and n can be a better secondary proxy.

- We find a slight positive correlation between n and halo concentration c with postive $n-M_h$ relations. In contrast, the simulation results show that more massive halos are less concentrated due to their more frequent mergers at late universe. After controlling for both stellar mass and halo mass, we observe a slight strengthening of the $n-c$ dependence. This suggest that the n of galaxies may serve as an indicator for the secondary $M_h - c$ relation, which contributes to the scatter of general $M_h - c$ relation in simulations. We therefore infer that, at fixed stellar mass, more concentrated galaxies and their host halos form earlier and higher concentrations.

- Using the group catalog from Yang et al. (2021), we find that more concentrated central galaxies are located in richer galaxy clusters and have a higher average satellite galaxy number density around them.

- TNG300 and SIMBA simulations qualitatively reproduce the positive correlation between n and halo mass as well as richness, but the correlation in TNG300 is very weak. Additionally, neither simulation shows positive $n-c$ relationships. By further controlling halo mass in the TNG300 sample, we find a weak positive $n-c$ correlation.

- In TNG300 and SIMBA, there are slight positive correlations between n and black hole mass, and strong positive correlations between black hole mass and halo mass. As we progressively turn off X-ray feedback and jet-mode AGN feedback in SIMBA simulations, the correlation between n and halo mass gradually disappeared. This suggests that AGN feedback plays a critical role in the halo mass dependence on secondary galaxy properties mentioned above.

Our detection of the halo mass dependence on secondary galaxy properties bring better insights into the physics of galaxy assembly bias, which is an important problem in the current galaxy-halo connection field. With next-generation surveys and better measurements, the connection between galaxies and halos should be better constrained.
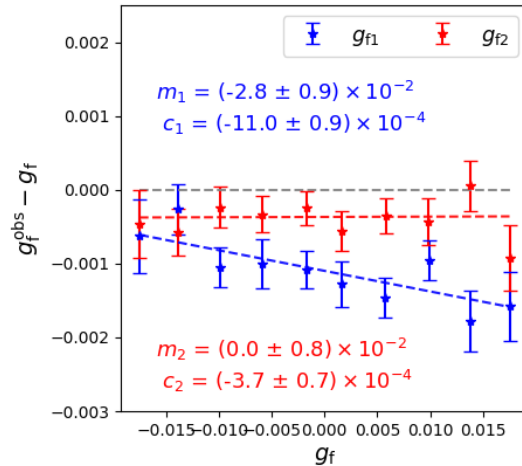
APPENDIX

A. FIELD DISTORTION TEST

Figure 10. Field distortion test. g_f represents the field distortion values from the shear catalog, while the vertical axis represents the difference between measured values g_f^{obs} and true values. Blue and red correspond to the two components of the shear. m_i and c_i represent the multiplicative and additive biases obtained from linear fitting, respectively.

Here, we measure the multiplicative biases introduced in shear measurements and correct it in our analysis. Such biases arise from systematic errors or the intrinsic noisiness of the shear estimators, and they are typically quantified linearly,

$$g^{\mathrm{obs}} = (1 + m_{\mathrm{bias}})g^{\mathrm{true}} + c_{\mathrm{bias}}, \tag{A1}$$

where m_{bias} is multiplicative bias and c_{bias} is addictive bias, g^{true} refers to the real shear and g^{obs} represents the measured shear. Field distortion (FD) refers to the deviations between the shape of images and the actual object shapes due to imperfections in the optical system or imaging equipment, manifesting as various forms of image distortion, stretching, or compression. Zhang et al. (2019) propose using the inherent distortion of the CCD focal plane to detect c_{bias} and m_{bias} in shear measurements. This is a calibration method based on the properties of the data itself, without the need for simulations or any external datasets. The FQ shear catalog provides the field distortion at the location of each galaxy, g_{f1} and g_{f2}. Galaxies, located at the same position on the exposure, have the same distortion, implying that their intrinsic shear signal is zero and only the FD signal is present. By comparing the measured field distortion signal with the true signal in the catalog, the shear bias in the measurements can be determined.

We perform a FD test on all background galaxies for all lens galaxies we used, with the results shown in Figure 10. To better match the galaxy-galaxy lensing scenario, we weight each background galaxy by Σ_c (Eq. 3). Figure 10 displays the measured signals for the two shear components, where g_{f} is the true FD value, and the vertical axis represents the difference between the observed distortion value $g_{\mathrm{f}}^{\mathrm{obs}}$ and the true value. The figure also shows the shear bias results obtained from fitting, revealing that the g_1 component is underestimated by about 3%. Consequently, we correct G_1 in the catalog as $G_1/(1 + m_1)$ before proceeding with subsequent lensing measurements. Additionally, c_{bias} is largely mitigated by rotating background galaxies toward the lenses during galaxy-galaxy lensing calculations, with further reduction through the subtraction of random point signals.

REFERENCES

Ahn, C. P., Alexandroff, R., Prieto, C. A., et al. 2012, The Astrophysical Journal Supplement Series, 203, 21

Alonso, P., Wang, W., Zhang, J., et al. 2023, The Astrophysical Journal, 947, 19, doi: 10.3847/1538-4357/acbf4a

Andreon, S., & Hurn, M. A. 2010, Monthly Notices of the Royal Astronomical Society, 404, 1922, doi: 10.1111/j.1365-2966.2010.16406.x

Bolton, A. S., Schlegel, D. J., Aubourg, É., et al. 2012, The Astronomical Journal, 144, 144

Bryan, G. L., & Norman, M. L. 1998, The Astrophysical Journal, 495, 80, doi: 10.1086/305262

Chen, M., Cui, W., Fang, W., & Wen, Z. 2024, The Astrophysical Journal, 966, 227, doi: 10.3847/1538-4357/ad3931

Chiu, I. N., Okumura, T., Oguri, M., et al. 2020, Monthly Notices of the Royal Astronomical Society, 498, 2030, doi: 10.1093/mnras/staa2440

Christensen, N., & Meyer, R. 2000, arXiv e-prints, astro, doi: 10.48550/arXiv.astro-ph/0006401

Cooper, M. C., Gallazzi, A., Newman, J. A., & Yan, R. 2010, MNRAS, 402, 1942, doi: 10.1111/j.1365-2966.2009.16020.x

Correa, C. A., Wyithe, J. S. B., Schaye, J., & Duffy, A. R. 2015, Monthly Notices of the Royal Astronomical Society, 452, 1217

Cui, W., Davé, R., Peacock, J. A., Anglés-Alcázar, D., & Yang, X. 2021, Nature Astronomy, 5, 1069

Davé, R., Anglés-Alcázar, D., Narayanan, D., et al. 2019, Monthly Notices of the Royal Astronomical Society, 486, 2827

Davis, B. L., Graham, A. W., & Cameron, E. 2019, The Astrophysical Journal, 873, 85

Diemer, B. 2018, The Astrophysical Journal Supplement Series, 239, 35

Diemer, B. 2022, Monthly Notices of the Royal Astronomical Society, 513, 573, doi: 10.1093/mnras/stac878

Duffy, A. R., Schaye, J., Kay, S. T., & Dalla Vecchia, C. 2008, Monthly Notices of the Royal Astronomical Society: Letters, 390, L64

Eisenstein, D. J., & Hu, W. 1998, The Astrophysical Journal, 496, 605, doi: 10.1086/305424

Fong, M., & Han, J. 2021, Monthly Notices of the Royal Astronomical Society, 503, 4250, doi: 10.1093/mnras/stab259

Gao, H., Han, J., Fong, M., Jing, Y. P., & Li, Z. 2023, The Astrophysical Journal, 953, 37, doi: 10.3847/1538-4357/acdfcd

Guo, H., Yang, X., Raichoor, A., et al. 2019, The Astrophysical Journal, 871, 147

He, J., Wang, W., Li, Z., et al. 2024, arXiv e-prints, arXiv:2407.14827, doi: 10.48550/arXiv.2407.14827

Johnston, D. E., Sheldon, E. S., Wechsler, R. H., et al. 2007, arXiv e-prints, arXiv:0709.1159, doi: 10.48550/arXiv.0709.1159

Li, H., & Zhang, J. 2021, The Astrophysical Journal, 911, 115, doi: 10.3847/1538-4357/abec6d

Liu, C., Zhang, J., Li, H., Vaquero, P. A., & Wang, W. 2024. https://arxiv.org/abs/2407.00370

Ludlow, A. D., Bose, S., Angulo, R. E., et al. 2016, Monthly Notices of the Royal Astronomical Society, 460, 1214

Ludlow, A. D., Navarro, J. F., Angulo, R. E., et al. 2014, Monthly Notices of the Royal Astronomical Society, 441, 378

Maccio, A. V., Dutton, A. A., Van Den Bosch, F. C., et al. 2007, Monthly Notices of the Royal Astronomical Society, 378, 55

Mandelbaum, R., Seljak, U., & Hirata, C. M. 2008, Journal of Cosmology and Astroparticle Physics, 2008, 006

Mandelbaum, R., Wang, W., Zu, Y., et al. 2016, MNRAS, 457, 3200, doi: 10.1093/mnras/stw188

McConnell, N. J., & Ma, C.-P. 2013, The Astrophysical Journal, 764, 184

McLure, R. J., & Dunlop, J. 2002, Monthly Notices of the Royal Astronomical Society, 331, 795

More, S., van den Bosch, F. C., Cacciato, M., et al. 2011, Monthly Notices of the Royal Astronomical Society, 410, 210, doi: 10.1111/j.1365-2966.2010.17436.x

Moster, B. P., Naab, T., & White, S. D. M. 2018, Monthly Notices of the Royal Astronomical Society, 477, 1822, doi: 10.1093/mnras/sty655

Murata, R., Nishimichi, T., Takada, M., et al. 2018, The Astrophysical Journal, 854, 120, doi: 10.3847/1538-4357/aaaab8

Murata, R., Oguri, M., Nishimichi, T., et al. 2019, Publications of the Astronomical Society of Japan, 71, 107, doi: 10.1093/pasj/psz092

Navarro, J. F., Frenk, C. S., & White, S. D. 1997, The Astrophysical Journal, 490, 493

Nishizawa, A. J., Hsieh, B.-C., Tanaka, M., & Takata, T. 2020, arXiv preprint arXiv:2003.01511

Peng, Y.-j., Lilly, S. J., Renzini, A., & Carollo, M. 2012, The Astrophysical Journal, 757, 4, doi: 10.1088/0004-637X/757/1/4

Phriksee, A., Jullo, E., Limousin, M., et al. 2020, Monthly Notices of the Royal Astronomical Society, 491, 1643, doi: 10.1093/mnras/stz3049

Pillepich, A., Springel, V., Nelson, D., et al. 2017, Monthly Notices of the Royal Astronomical Society, 473, 4077, doi: 10.1093/mnras/stx2656

Posti, L., & Fall, S. M. 2021, A&A, 649, A119, doi: 10.1051/0004-6361/202040256

Rodríguez-Puebla, A., Avila-Reese, V., Yang, X., et al. 2015, The Astrophysical Journal, 799, 130, doi: 10.1088/0004-637X/799/2/130

Rodríguez Montero, F., Davé, R., Wild, V., Anglés-Alcázar, D., & Narayanan, D. 2019, Monthly Notices of the Royal Astronomical Society, 490, 2139, doi: 10.1093/mnras/stz2580

Rozo, E., Rykoff, E. S., Evrard, A., et al. 2009, The Astrophysical Journal, 699, 768, doi: 10.1088/0004-637X/699/1/768

Sérsic, J. 1963, Boletin de la Asociacion Argentina de Astronomia La Plata Argentina, 6, 41

Shen, Z., Zhang, J., Liu, C., et al. 2024, Tele-Correlation: Calibrating Shear-Shear Correlation with Real Data. https://arxiv.org/abs/2406.17991

Simet, M., McClintock, T., Mandelbaum, R., et al. 2017, Monthly Notices of the Royal Astronomical Society, 466, 3103, doi: 10.1093/mnras/stw3250

Sonnenfeld, A., Wang, W., & Bahcall, N. 2019, Astronomy & Astrophysics, 622, A30

Taylor, E. N., Cluver, M. E., Duffy, A., et al. 2020, Monthly Notices of the Royal Astronomical Society, 499, 2896

Thomas, N., Davé, R., Anglés-Alcázar, D., & Jarvis, M. 2019, Monthly Notices of the Royal Astronomical Society, 487, 5764

Tinker, J. L., Cao, J., Alpaslan, M., et al. 2021, Monthly Notices of the Royal Astronomical Society, 505, 5370, doi: 10.1093/mnras/stab1576

Tinker, J. L., Leauthaud, A., Bundy, K., et al. 2013, The Astrophysical Journal, 778, 93

Tinker, J. L., Robertson, B. E., Kravtsov, A. V., et al. 2010, The Astrophysical Journal, 724, 878

Wandel, A. 2002, The Astrophysical Journal, 565, 762

Wang, W., & White, S. D. M. 2012, Monthly Notices of the Royal Astronomical Society, 424, 2574, doi: 10.1111/j.1365-2966.2012.21256.x

Wang, W., Li, X., Shi, J., et al. 2021, The Astrophysical Journal, 919, 25

Wang, W., Li, X., Shi, J., et al. 2021, The Astrophysical Journal, 919, 25, doi: 10.3847/1538-4357/ac0e38

Weinberger, R., Springel, V., Pakmor, R., et al. 2018, Monthly Notices of the Royal Astronomical Society, 479, 4056, doi: 10.1093/mnras/sty1733

Xu, K., & Jing, Y. 2022, The Astrophysical Journal, 926, 130

Xu, K., Jing, Y. P., Zheng, Y., & Gao, H. 2023, The Astrophysical Journal, 944, 200, doi: 10.3847/1538-4357/acb13e

Xu, K., Zheng, Y., & Jing, Y. 2022, The Astrophysical Journal, 925, 31, doi: 10.3847/1538-4357/ac38a2

Yang, X., Mo, H. J., van den Bosch, F. C., et al. 2006, Monthly Notices of the Royal Astronomical Society, 373, 1159, doi: 10.1111/j.1365-2966.2006.11091.x

Yang, X., Xu, H., He, M., et al. 2021, The Astrophysical Journal, 909, 143

Zentner, A. R., Hearin, A. P., & van den Bosch, F. C. 2014, MNRAS, 443, 3044, doi: 10.1093/mnras/stu1383

Zhang, J. 2008, Monthly Notices of the Royal Astronomical Society, 383, 113, doi: 10.1111/j.1365-2966.2007.12585.x

Zhang, J., Zhang, P., & Luo, W. 2016, The Astrophysical Journal, 834, 8, doi: 10.3847/1538-4357/834/1/8

Zhang, J., Dong, F., Li, H., et al. 2019, The Astrophysical Journal, 875, 48, doi: 10.3847/1538-4357/ab1080

Zhao, D., Jing, Y., Mo, H., & Börner, G. 2009, The Astrophysical Journal, 707, 354

Zu, Y., Shan, H., Zhang, J., et al. 2021, MNRAS, 505, 5117, doi: 10.1093/mnras/stab1712

Zu, Y., Song, Y., Shao, Z., et al. 2022, MNRAS, 511, 1789, doi: 10.1093/mnras/stac125